Submitted to small

DOI: 10.1002/smll.201303051R1
Article type: ((Full Paper))

Multifunctional Inverted Nanocone Arrays for Non-wetting, Self-cleaning Transparent Surface with High Mechanical Robustness

*Jeong-Gil Kim, Hyungryul J. Choi, Kyoo-Chul Park, Robert E. Cohen, Gareth H. McKinley, and George Barbastathis**

J.-G. Kim, H. J. Choi, Dr. K.-C. Park, Prof. G. H. McKinley and Prof. G. Barbastathis
Department of Mechanical Engineering, Massachusetts Institute of Technology
Cambridge, Massachusetts, 02139 (United States)
E-mail: ((gbarb@mit.edu))

Prof. G. Barbastathis
Singapore-MIT Alliance for Research and Technology (SMART) Centre
Singapore 138602 (Singapore)

Prof. R. E. Cohen
Department of Chemical Engineering, Massachusetts Institute of Technology
Cambridge, Massachusetts, 02139 (United States)

Keywords: ((Nanostructures, Mechanical properties, Self-cleaning, Anti-fogging, Anti-reflectivity))

Abstract: A multifunctional surface that enables control of wetting, optical reflectivity and mechanical damage of nanostructured interfaces is presented. Our approach is based on imprinting a periodic array of nanosized cones into a UV-curable polyurethane acrylate (PUA), resulting in a self-reinforcing egg-crate topography evenly distributed over large areas up to several cm^2 in size. The resulting surfaces can be either superhydrophilic or superhydrophobic (through subsequent application of an appropriate chemical coating), they minimize optical reflection losses over a broad range of wavelengths and a wide range of angles of incidence, and they also have enhanced mechanical resilience due to greatly improved redistribution of the normal and shearing mechanical loads. The transmissivity and wetting characteristics of the nanoscale egg-crate structure, as well as its resistance to mechanical deformation are analyzed theoretically. Experiments show that the optical performance together with self-cleaning or anti-fogging behavior of the inverted nanocone topography is comparable to earlier designs that have used periodic arrays of nanocones to control reflection and wetting. However the egg-crate structures are far superior in terms of mechanical robustness, and the ability to replicate this topography through several generations is promising for large-scale commercial applications where multifunctionality is important.

1. Introduction

Control of interfacial physical phenomena across multiple modalities, for example optical reflection and surface wettability, is increasingly important both from the point of view of fundamental understanding of interfacial properties and of course for engineering applications. For example, eliminating reflection at an air-glass interface increases the efficiency of light-harvesting devices and display devices.[1] These same surfaces must also meet stringent requirements of anti-fogging due to condensation or, in other cases, must be self-cleaning to avoid accumulation of dust and other particulate contaminants with low risk of mechanical damage.[2] In the former case, superhydrophilicity of the surfaces prevents fogging by rapidly wicking deposited droplets into the surface texture and transforming them into a thin uniform layer of water that rapidly evaporates;[2c, 3] whereas in the latter case, superhydrophobicity helps to remove dust from the surface through the action of water droplets that collect the dust particles and then roll off carrying particulate matter with them.[4] These behaviors are often referred to as "anti-fogging" and "self-cleaning," respectively.[5]

Engineered surfaces that combine these modal responses are commonly referred to as "multifunctional," and considerable research effort has been invested in their design, fabrication, replication, and characterization.[6] Such surfaces are commonly encountered in nature as observed for example in the anti-reflectivity of moth eyes[7] and the super-hydrophobicity of lotus leaves that in turn enables self-cleaning.[2a-c, 8]

Recently, we have developed a biomimetic multi-functional silica surface by utilizing a square array of slender tapered nanocone structures with pitch of $P \approx 200$ nm and an aspect ratio (defined as the ratio of nanocone height to pitch) of $H/P \approx 5$. We demonstrated broadband ($400 \text{ nm} \leq \lambda \leq 1200 \text{ nm}$) omnidirectional ($0° \leq \theta_{\text{incidence}} \leq 75°$) anti-reflectivity and robust superhydrophobicity. We also quantified the anti-fogging behavior resulting from the superhydrophilicity of the same nanotextured surface, by employing the intrinsic hydrophilicity of glass.[6c] From the point of view

of optical behavior, the nanocones act in a similar way to an anechoic chamber, providing adiabatic impedance matching between the air and the glass and thus significantly reducing Fresnel reflection losses. When exposed to water vapor, the nanocone structures exhibit superhydrophilicity due to the hydrophilic nature of glass in conjunction with high surface roughness arising from the steep nanocone structure. This promotes the rapid formation of a thin conformal film of water instead of the familiar condensation droplets that result in excessive scattering. Conversely, superhydrophobicity can also be achieved on the same textured surface when combined with an additional hydrophobic coating (e.g. fluorosilane) resulting in a self-cleaning surface.[5a]

With regard to quantifying performance, we demonstrated that a single figure of merit: i.e., the nanocone slenderness, or height-to-pitch aspect ratio *(H/P)*, suffices to characterize both behaviors. The taller the cones and the smaller their diameter, the more gradual the adiabatic refractive index transition is and the more removed the reflection becomes from the diffractive regime; both qualities contribute to reducing reflection and scatter from the surface. Slender nanocone structure ($H/P >> 1$) combined with a small hemispherical tip radius ($R_{tip} \cong 17$ nm) leads to high Wenzel roughness ($r_W \cong 9.7$).[2c] When combined with a suitable fluorinated chemical coating, the high aspect ratio of the features and the small area fraction of the conical tips promote development of a very stable superhydrophobic Cassie-Baxter state with very low contact angle hysteresis.

However, the slender mechanical structures of needles and nanocones are subject to high risk of mechanical damage. As one would intuitively expect, and as we verify with detailed numerical calculations below, the slender nanocones are very sensitive to damage from stresses arising from external loading through direct mechanical contact or capillary action.[9] Lack of mechanical robustness makes transparent nanocone surfaces inappropriate for several applications of importance, for example surfaces of personal digital assistants (PDAs) or cell phones that are subject to repeated shearing and normal loads due to finger-swiping motions by the user.

Here, we utilize a square array of inverted nanocones, which we refer to as nanoholes arranged in "egg-crate structures" on a substrate[10] to achieve similar anti-reflection and anti-fogging or self-cleaning behavior. As has been pointed out in previous works employing imprint-assisted replication of cones into polydimethylsiloxane (PDMS),[11] the complementary topographic structure of nanoholes is amenable to a high throughput nano-replication method that uses an array of cones as a 'negative' master. We use our high-aspect ratio fabrication technique[6c] to make the nanocone masters and a UV-cured nanoreplication process on poly urethane acrylate (PUA) that results in egg-crate structures much harder than PDMS. The aspect ratio of the nanohole arrays we can achieve is approximately as high as the original nanocone structures and, hence, our nanoreplicas exhibit broadband optical transmissivity that is almost identical with the original nanocone structures, whilst still retaining anti-fogging or self-cleaning properties. The egg-crate topography results in a radical improvement in mechanical robustness of the nanoreplicated structures. In following sections we present numerical simulations of the optical, mechanical and wetting properties, as well as experimental measurements of the corresponding properties on nanoreplicated samples.

2. Results and Discussion

2.1 Numerical Models of Mechanical Robustness, Optical and Wetting Behaviors

In this section, we first discuss quantitatively the multi-functional device aspects of the inverted nanocone array, namely anti-reflection and wetting, in the context of mechanical robustness. As briefly mentioned in Section 1, the low optical reflectivity of our design arises mainly due to an axially-varying effective refractive index of the tapered structures on a length scale that is below the wavelength of incident irradiation. The effective gradient introduced by the tapered nanostructures effectively eliminates the abrupt discontinuity in the refractive index at the interface between the substrate and air, thus suppressing Fresnel reflection. This effective gradient in the refractive index

is equally applicable to both of the periodic nanostructures we have described (i.e. either cones or holes), and in this section we show numerically that indeed they both reduce reflective losses by a similar extent.

We calculated the reflection of plane waves at different wavelengths (350 nm ≤ λ ≤ 1800 nm) at normal incidence through the nanostructured surfaces using FDTD (Finite-difference time-domain) based software (FDTD Solutions 8.0). Results are shown in Figure 1A and 1B for nanocone arrays, as well as for the inverse geometry consisting of an array of tapered cavities. The structures were simulated as square arrays with pitch of P = 200 nm and varying aspect ratio (H/P). For structures with higher aspect ratio, anti-reflectivity on the surface is enhanced because the gradient of the effective refractive index becomes progressively smaller and more consistent with the adiabatic assumption. Especially when the aspect ratio exceeds $H/P \geq 3$, the reflective loss at a zero incidence angle can be suppressed to less than 1% over our entire range of wavelengths used in our simulation.

Turning to the wetting behavior, the tapered hole geometry resulting from the inverted nanocone array structure also amplifies the interfacial thermodynamic driving force that governs the surface wettability. This structural effect can either increase the intrinsic hydrophilicity of the untreated poly urethane acrylate (PUA) or enhance the Cassie-Baxter hydrophobicity of the textured nanohole surface after applying a fluorosilane coating (see Experimental Section for details). Figures 2A and 2B show the resulting energy landscapes for different putative apparent contact angles (θ_p^*) and vertical (z) locations of the water meniscus in the nanohole, calculated from the three-dimensional topography (shown in Figure 1B) and for two different equilibrium contact angles, corresponding to θ_E = 80° for untreated PUA, and θ_E = 120° for fluorosilane coated PUA.[12] The blue color represents the locus of the global minimum for the change in the Gibbs free energy density in each plot (See Supporting Information for details of the relevant Gibbs free energy density function), which predicts that the system corresponding to the apparent contact angle is thermodynamically

stable. The fully-wetted state and the resulting extremely low apparent contact angle of the untreated PUA nanostructure ($\theta^* < 5°$) can be described by the canonical Wenzel relation $\cos\theta^* = r_W\cos\theta_E$,[13] where θ^* and θ_E are the apparent and equilibrium contact angles for water drops on textured and smooth PUA surfaces, respectively, and r_W is the roughness ratio between the total surface area and the corresponding projected area. Water spontaneously wicks into the nanohole geometry because the intrinsic hydrophilicity of the untreated PUA surface is amplified by the roughness and leads to an inwardly-directed net capillary force that acts on the curved meniscus in each nanohole. Thermodynamically, the resulting water-solid interface that replaces the initial dry air-solid interface and the liquid meniscus has a lower total change in the Gibbs free energy density.[12a] The energetically favorable formation of a thin conformal film of water resulting from rapid wicking into the nanostructure provides the strong anti-fogging property[14] that is observed experimentally in section 2.2. On the other hand, the global minimum of the Gibbs free energy density variation for the hydrophobically-modified inverted nanocone structure predicts a composite or Cassie-Baxter state in which the water droplet sits partially on the peaks of the wetted solid texture and partially on a raft of air pockets trapped in the nanoholes. The apparent contact angle of the water droplet can be modeled by the Cassie-Baxter relation, $\cos\theta^* = r_\phi\phi_s\cos\theta_E - (1-\phi_s)$,[12a, 15] where $r_\phi = (1-\pi/4) + \pi/2 \times \left[1-(1-z/H)^2\right]\sqrt{(H/P)^2+1/4}$ is the roughness of the actual wetted area and $\phi_s = 1-(\pi/4)(1-z/H)^2$ is the area fraction of the water-air interface occluded by the texture.[12b, 15c] It should be noted that r_ϕ and ϕ_s are functions of z/H. The apparent contact angle of $\theta^* = 156°$ resulting from the Gibbs free energy density variation calculation in Figure 2B matches well the experimental measurement results shown in the inset. The high feature density (corresponding to the number of asperities in 1 mm^2) and the closed nature of the inverted nanocone structure lead to a highly robust Cassie-Baxter state[16] (See Supporting Information for details).

The enhancement in the wetting characteristics, attributed to the tapered nature of the high feature density η of the nanocones, improves further as the aspect ratio (H/P) increases, just as in the case of optical transmissivity of the nanocones.[6c] Nevertheless, there is an evident trade-off between the performance characteristics of these high aspect ratio and high feature density conical structures and the resulting mechanical robustness of the texture. Assuming the same basal area (i.e. the same feature density), the more slender the cone, the smaller the maximum applied force the cone can resist before a critical stress for mechanical failure is attained under external loading. On the other hand, a square array of nanohole structures forms an egg-crate like structure, which is intuitively expected to withstand larger external loads, since the walls of the nanoholes abut each other in a two-dimensional network. We simulated and quantitatively compared both the compressive stress, the shear stress and the strain field resulting from comparable external forces applied to both the nanocone and nanohole cases using finite element method based software (ANSYS). The results are shown in Figure 3. In both the nanocone and nanohole geometries, the simulated geometry consisted of a square array with a pitch of P = 200 nm and aspect ratio of H/P = 4. The material (PUA) was assumed to be isotropic and perfectly elastic with modulus $E \approx 400$ MPa. The external force applied to the nanostructured surface is set to be 4 N over a circular area with a radius of 5 mm corresponding to an applied load of 2 pN per a single cone or hole, comparable to what might result from a single finger pressing uniformly on the nanotextured surface.[17] When a normal force is applied to the nanocone structures, the stress is clearly concentrated at the conical tips of the features, whereas for nanoholes the external load is much more evenly distributed over the entire top surface area as shown in Figure 3A; the stress is therefore lower throughout the structure. The maximum Von Mises stresses are $\sigma_{max,\,shear}$= 50.4 MPa and $\sigma_{max,\,normal}$ = 44.8 MPa for the nanocones and $\sigma_{max,\,shear}$= 1.34 MPa and $\sigma_{max,\,normal}$ = 1.23 MPa for the nanoholes, respectively. In particular for the nanocones, the maximum stress exceeds the reported bulk yield stress of the PUA material ($\sigma_y \approx$ 17 MPa).[18] Although systematic scale-dependent changes in the magnitude of the yield stress in

nanoscale-modulated structures is a subject of open investigation,[19] reaching values of peak stress in the proximity of the nominal or bulk yielding value creates concern about plastic deformation, fracture and subsequent degradation in both optical and wetting performance. Alternatively, one may also look at the lateral displacement of the textured elements that comprise the multifunctional surface: For a nanocone structure with aspect ratio of $H/P = 4$, application of a 4 N shear force over the array results in a tip deflection of δ_{tip} = 148 nm, which is larger than the half pitch ($P/2$ = 100 nm). The large shear strain is certain to lead to irreversible collapse of the periodic nanostructure. On the other hand, the walls of the nanohole egg-crate array exhibit a very small deflection ($\delta < 0.1$ nm) when subjected to the same magnitude and direction of force. In addition, unlike the slender nanocones, the nanohole egg-crate structures are expected to be free from buckling and collapse problems.

2.2 Experimental Results and Discussion

In Figure 4 we show scanning electron microscope (SEM) images of a mold of nanocone arrays fabricated using laser interference lithography, replicated nanohole arrays on a PUA surface and also second generation replicated nanocone structures on a PUA surface. The fabricated nanocone and nanohole arrays each have a pitch of 200 nm and aspect ratio 4:1.

Measured transmission spectra under normal incidence for the inverted nanocone and the nanocone arrays are shown in Figure 5A. Measurements of the transmission spectra were carried out using a spectrophotometer (Varian Cary-500i) in the visible to near infrared range (350 nm < λ < 1400 nm). Both the tapered nanocone and nanohole arrays exhibit enhanced optical transmittance when compared to a flat fused silica surface over the range from 450 nm to 1400 nm due to the combined effects of the tapered geometry and the high aspect ratio of the features. This is consistent with the numerical calculations shown in Figures 1A and 1B. In Figure 5B we show the enhanced optical transmission (T) of the replicated egg-crate patterns at different incident angles from 0° to 80° with

transverse electric (TE) polarized irradiation at a wavelength of λ = 633 nm. At angles of θ_i = 0°, 40°and 80°, the transmissivity of the nanohole egg-crate array is T = 95.9%, 90.6% and 40.3% respectively, but these values drop to T = 93.2%, 86.8% and 23.0% respectively for the flat silica glass. While lower optical transmission at larger incidence angles is expected for both for the flat surface and the egg-crate patterned surface due to the physics of reflection, the egg-crate patterned surface persistently exhibits higher transmissivities than the corresponding flat glass surface, even at very high incidence angles.

The superhydrophilicity of the nanotextured egg-crate surface shown in the inset of Figure 2A results in anti-fogging behavior via the formation of a thin wetting film of water that fills the nanotexture and prevents the formation of micrometric water droplets on the surface that subsequently scatter light. The anti-fogging behavior is quantified by measuring the 0^{th} order optical transmission of laser (λ = 633 nm) at normal incidence through both a nanotextured surface and a control surface consisting of a cleaned glass slide, each of which is exposed to a stream of saturated steam (flow velocity $V \cong$ 3 m/s and temperature of 87.6 ºC). As shown in Figure 6A, the nanotextured film exhibits a reduction in transmission of less than $\Delta T \cong$ 4%, whereas the cleaned glass slide shows a sudden large drop of transmission $\Delta T \cong$ 94% when placed in the stream of steam because light is scattered from the microscopic fog droplets that are deposited on the glass surface. The slow evaporation of these pinned droplets also results in a longer time to recover complete transmission compared to the nanotextured surface.

The strong water-repellency of fluorosilane-treated tapered nanohole structure also confers self-cleaning properties to these surfaces. Water droplets ($V \approx$ 10 μL) were dispensed every 5 seconds onto two kinds of samples that were inclined with a tilting angle of α = 30° (Figure 6B) and covered with three different kinds of common micrometric contaminants (silicon carbide, lycopodium spores and white sand, with average diameters of 10 μm, 30 μm and 100 μm, respectively). The change in the optical transmission with the number of droplets dispensed on the

samples is shown in Figure 6B to illustrate how easily the water droplets can remove different particulate contaminants from the nanotextured surfaces. When compared to the cleaned glass slide, the water-repellent nanotextured surface exhibits nearly no residual contaminants, and we observe full recovery of optical transmission after 3-5 drops of water impact the surface.

The mechanical robustness of a PUA surface textured with the nanoholes was also tested experimentally. First, a tapping force of 4 N was applied to the sample along the normal and shear directions of the nanotextured surface through a latex rubber pad (McMaster-Carr, 85995K28) with dimensions 8.9 mm by 8.9 mm repeatedly. Each contact pressing consisted of 5 seconds of force application corresponding to an applied normal stress of 50 kPa. Figure 7A shows that there is nearly no degradation of optical transmission after repeated loading conditions up to 50 times. Alternatively pressing the sample with higher force up to 60 N through a Neoprene rubber ball (McMaster-Carr, 1241T4, Young's modulus $E_{np} \cong 5.5$ MPa, radius $R_{np} = 4.8$ mm) resulted in small degradation of the sample in terms of optical transmission. Small distortions of structures at the top surface are observed as shown in the inset of the graph. The optical performance started to degrade at 60 N of loading, (corresponding to pressure of 3 MPa, calculated using Hertz contact pressure[20]), due to distortion of the periodicity in the hole array at the top surface, as shown in the inset of Figure 7B.

3. Conclusion

We have demonstrated a replication-based approach using a UV photocurable polymer capable of mass-producing multifunctional nanostructured films consisting of periodic arrays of inverted nanoholes in an egg-crate structure. These textured structures have superior anti-reflective and wetting properties compared to flat fused silica glass surfaces and enjoy greater mechanical robustness than our earlier approach.[6c] While retaining the high feature density and high aspect ratio characteristics of tapered nanostructures that provide multifunctional enhancement of both the

optical and wetting performance, the nanohole arrays also provide high mechanical robustness regardless of their aspect ratio via stress redistribution across a broad network of interconnected features. The UV replication method is compatible with large area imprint[21] or roll-to-roll processes,[22] offering potential advantages such as low cost and high throughput. With such processes, it can be anticipated that multifunctional surfaces can be fabricated in the form of flexible plastic films and thus applied conformally as an adhesive tape to a broad range of materials such as glass, silicon and other optical plastics. The process is also compatible with curved substrates. These nanohole egg-crate structures and the ability to continuously manufacture structures using roll-to-roll process technology may offer potential for industrial applications that require combined control of reflectivity and wetting behavior over large surface areas, such as photovoltaic cells, car windshields and future touch-screen display devices.

4. Experimental Section

As a first step of the replication process, a master mold (40 mm by 40 mm) comprising of a periodic array of nanoconical features was prepared using laser interference lithography and subsequent dry etching steps with multiple shrinking masks as described previously.[6c] Using the master nanocone array as a negative mold for the nanohole array, the UV replication process was performed using the sequence of operations shown in Figure 8A. First, the master mold was placed in contact and pushed onto a poly urethane acrylate (PUA) prepolymer (311 RM, Minuta Tech.) dispensed via syringe on a glass substrate. After curing the PUA with ultra-violet (UV) light (Tamarack UV exposure system; with peak wavelength and intensity of 365 nm and 4.5 mW/cm^2 respectively), the mold was carefully detached from the PUA surface. In order to enhance the adhesion between the imprinted PUA and the fused silica substrate, a silane-type adhesion promoter layer[23] was applied. Thus the periodic nanocone arrays on the mold were inversely replicated into the PUA surface, texturing it with a periodic array of nanoholes. This replicated egg-crate structure was subjected to

an additional imprint step resulting in a second generation textured PUA surface composed of nanocone arrays as shown in Figure 8B. This second replication was carried out in order to compare the topography and performance of the inverted nanocone arrays with that of the original nanocone arrays. In the second imprint, a PDMS anti-adhesion layer[24] was first coated on the mold surface to prevent the two PUA layers from irreversibly fusing into each other. Also, a vacuum-assisted filling process was employed when the nanohole arrays were pressed into the liquid polymer in order to fully fill the nanoholes with PUA prepolymer during the second imprint step.[25] To lower the surface energy of the nanohole arrays and make the egg-crate structure strongly hydrophobic, chemical vapor deposition of 1*H*,1*H*,2*H*,2*H*-perfluorodecyltrichlorosilane (Alfa Aesar, 96%) has carried out in an oven at 110 °C for 10 hours.

Supporting Information
Supporting Information is available online from the Wiley Online Library.

Acknowledgments
We would like to thank the staff and facility support from the Nano Structures Laboratory, Microsystems Technology Laboratory, and Center for Materials Science and Engineering at MIT. This work was supported in part by the MIT Institute for Soldier Nanotechnologies (ISN) with the U.S. Army Research Office and by the Singapore National Research Foundation (NRF) through the Singapore-MIT Alliance for Research and Technology (SMART) Centre. J.-G. Kim thanks Samsung Electronics for financial support. H. J. Choi also thanks Kwanjeong Educational Foundation Scholarship for financial support.

Received: ((will be filled in by the editorial staff))
Revised: ((will be filled in by the editorial staff))
Published online on ((will be filled in by the editorial staff))

References

[1] a) C. H. Sun, P. Jiang, B. Jiang, *Appl. Phys. Lett.* **2008**, *92*, 061112; b) J. W. Leem, Y. M. Song, J. S. Yu, *Opt. Express* **2011**, *19*, A1155; c) Y. F. Li, J. H. Zhang, B. Yang, *Nano Today* **2010**, *5*, 117.

[2] a) B. Bhushan, Y. C. Jung, K. Koch, *Philos. Trans. R. Soc., A* **2009**, *367*, 1631; b) M. Nosonovsky, B. Bhushan, *Microsyst. Technol.* **2005**, *11*, 535; c) D. Quéré, *Annu. Rev. Mater. Res.* **2008**, *38*, 71; d) Y. C. Jung, B. Bhushan, *ACS Nano* **2009**, *3*, 4155; e) B. Bhushan, K. Koch, Y. C. Jung, *Appl. Phys. Lett.* **2008**, *93,* 093101; f) T. L. Sun, L. Feng, X. F. Gao, L. Jiang, *Acc. Chem. Res.* **2005**, *38*, 644.

[3] F. C. Cebeci, Z. Z. Wu, L. Zhai, R. E. Cohen, M. F. Rubner, *Langmuir* **2006**, *22*, 2856.

[4] W. Barthlott, C. Neinhuis, *Planta* **1997**, *202*, 1.

[5] a) R. Blossey, *Nat. Mater.* **2003**, *2*, 301; b) A. Otten, S. Herminghaus, *Langmuir* **2004**, *20*, 2405.

[6] a) W. L. Min, B. Jiang, P. Jiang, *Adv. Mater.* **2008**, *20*, 3914; b) J. Zhu, C. M. Hsu, Z. F. Yu, S. H. Fan, Y. Cui, *Nano Lett.* **2010**, *10*, 1979; c) K. C. Park, H. J. Choi, C. H. Chang, R. E. Cohen, G. H. McKinley, G. Barbastathis, *ACS Nano* **2012**, *6*, 3789.

[7] a) P. Vukusic, J. R. Sambles, *Nature* **2003**, *424*, 852; b) Y. Kanamori, M. Sasaki, K. Hane, *Opt. Lett.* **1999**, *24*, 1422; c) G. Xie, G. Zhang, F. Lin, J. Zhang, Z. Liu, S. Mu, *Nanotechnology* **2008**, *19*, 095605; d) Y. F. Huang, S. Chattopadhyay, Y. J. Jen, C. Y. Peng, T. A. Liu, Y. K. Hsu, C. L. Pan, H. C. Lo, C. H. Hsu, Y. H. Chang, *Nat. Nanotechnol.* **2007**, *2*, 770; e) K. Choi, S. H. Park, Y. M. Song, Y. T. Lee, C. K. Hwangbo, H. Yang, H. S. Lee, *Adv. Mater.* **2010**, *22*, 3713; f) A. Deinega, I. Valuev, B. Potapkin, Y. Lozovik, *J. Opt. Soc. Am. A* **2011**, *28*, 770; g) A. R. Parker, H. E. Townley, *Nat. Nanotechnol.* **2007**, *2*, 347.

[8] a) V. Zorba, E. Stratakis, M. Barberoglou, E. Spanakis, P. Tzanetakis, S. H. Anastasiadis, C. Fotakis, *Adv. Mater.* **2008**, *20*, 4049; b) A. Lafuma, D. Quéré, *Nat. Mater.* **2003**, *2*, 457.

[9] a) K. T. Lau, S. Q. Shi, H. M. Cheng, *Compos. Sci. Technol.* **2003**, *63*, 1161; b) E. J. Garcia, A. J. Hart, B. L. Wardle, A. H. Slocum, *Nanotechnology* **2007**, *18,* 165602; c) D. Chandra, S. Yang, *Acc. Chem. Res.* **2010**, *43*, 1080.

[10] a) A. Nakajima, K. Abe, K. Hashimoto, T. Watanabe, *Thin Solid Films* **2000**, *376*, 140; b) A. Nakajima, K. Hashimoto, T. Watanabe, *Monatsh Chem.* **2001**, *132*, 31; c) K. Choi, S. H. Park, Y. M. Song, C. Cho, H. S. Lee, *J. Mater. Chem.* **2012**, *22*, 17037.

[11] J. C. Woo, N. S. Baek, J. Y. Kim, C. I. Kim, *RSC Adv.* **2012**, *2*, 767.

[12] a) A. Marmur, *Langmuir* **2003**, *19*, 8343; b) A. Tuteja, W. Choi, J. M. Mabry, G. H. McKinley, R. E. Cohen, *Proc. Natl. Acad. Sci. USA* **2008**, *105*, 18200.

[13] R. N. Wenzel, *Ind. Eng. Chem.* **1936**, *28*, 988.

[14] a) M. Reyssat, L. Courbin, E. Reyssat, H. A. Stone, *J. Fluid Mech.* **2008**, *615*, 335; b) D. Lee, M. F. Rubner, R. E. Cohen, *Nano Lett.* **2006**, *6*, 2305.

[15] a) B. Krasovitski, A. Marmur, *Langmuir* **2005**, *21*, 3881; b) A. B. D. Cassie, S. Baxter, *Nature* **1945**, *155*, 21; c) A. J. B. Milne, A. Amirfazli, *Adv. Colloid Interface Sci.* **2012**, *170*, 48.

[16] C. Y. Jeong, C. H. Choi, *ACS Appl. Mater. Interfaces* **2012**, *4*, 842.

[17] S. A. Mascaro, H. H. Asada, *IEEE Trans. Rob. Autom.* **2004**, *20*, 26.

[18] M. Koshiba, K. K. S. Hwang, S. K. Foley, D. J. Yarusso, S. L. Cooper, *J. Mater. Sci.* **1982**, *17*, 1447.

[19] H. E. H. Meijer, L. E. Govaert, *Prog. Polym. Sci.* **2005**, *30*, 915.

[20] K. L. Johnson, *Contact Mechanics*, Cambridge University Press, Cambridge, United Kingdom **1985**.

[21] J. G. Kim, Y. Sim, Y. Cho, J. W. Seo, S. Kwon, J. W. Park, H. Choi, H. Kim, S. Lee, *Microelectron. Eng.* **2009**, *86*, 2427.

[22] S. H. Ahn, L. J. Guo, *ACS Nano* **2009**, *3*, 2304.

[23] D. E. Packham, *Handbook of adhesion, 2nd ed.*, Wiley, Hoboken, NJ, USA **2005**.

[24] M. J. Lee, N. Y. Lee, J. R. Lim, J. B. Kim, M. Kim, H. K. Baik, Y. S. Kim, *Adv. Mater.* **2006**, *18*, 3115.

[25] J. G. Kim, H. J. Choi, H. H. Gao, I. Cornago, C. H. Chang, G. Barbastathis, presented at the 2012 Int. Conf. on Optical MEMS and Nanophotonics, Banff, AB, August **2012**.

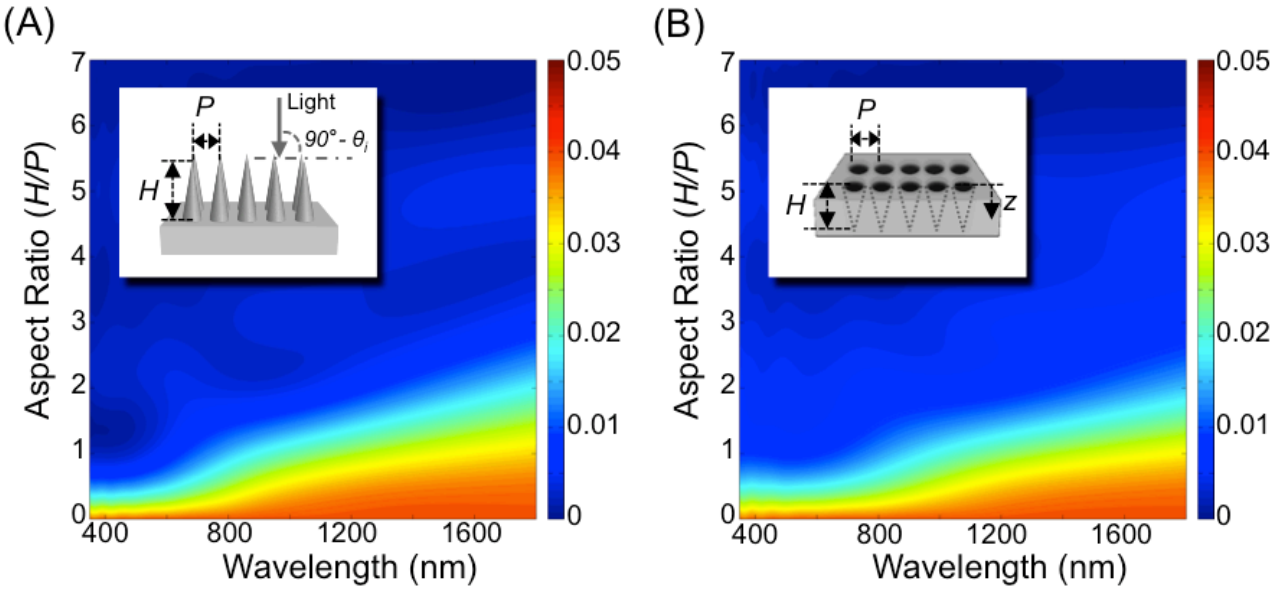

Figure 1. FDTD (Finite-difference time-domain) simulations of the optical performance of the nanostructured surfaces in the wavelength range of 350 nm $\leq \lambda \leq$ 1800 nm at normal incidence (θ_i = 0°): Contour plot of the fraction of light reflected $R(\lambda, H/P)$ from surfaces textured with either (A) nanocone arrays or (B) nanohole arrays.

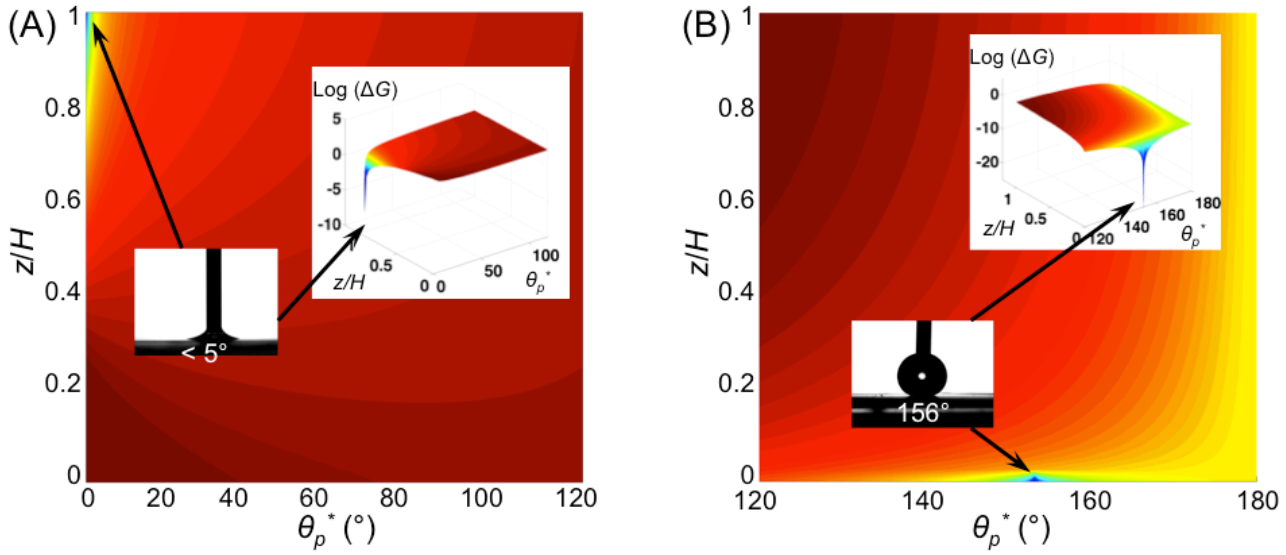

Figure 2. Colored contour maps of the change in the Gibbs free energy density $\Delta G(\theta_p^*)$ as a function of the putative apparent contact angle (θ_p^*) with a water droplet and different normalized vertical position (z/H) of the water meniscus in the inverted nanocone array (A) with intrinsically hydrophilic PUA (θ_E = 80°) and (B) with hydrophobic fluorosilane surface coating (θ_E = 120°). See Supporting Information for the Gibbs free energy density function. The effective apparent contact angle (θ^*) is related to the equilibrium contact angle (θ_E) by the Cassie-Baxter relation that accounts for the solid-liquid fraction and air-liquid fraction for liquid-solid-air composite state of droplet (in the limit of fully-wetted state ($z/H \rightarrow 1$), the Wenzel relation is used). r_ϕ and ϕ_s are functions of z/H. The insets show goniometric images of water droplets (V = 10 μl) sitting on each surface. In both (A) and (B), the blue color represents the locus of the global minimum in the Gibbs free energy density variation landscape and the corresponding apparent contact angles ($\theta^* = \theta_p^*$ when ΔG = min(ΔG)) are in good agreement with the experimental results measured by goniometry shown in the insets.

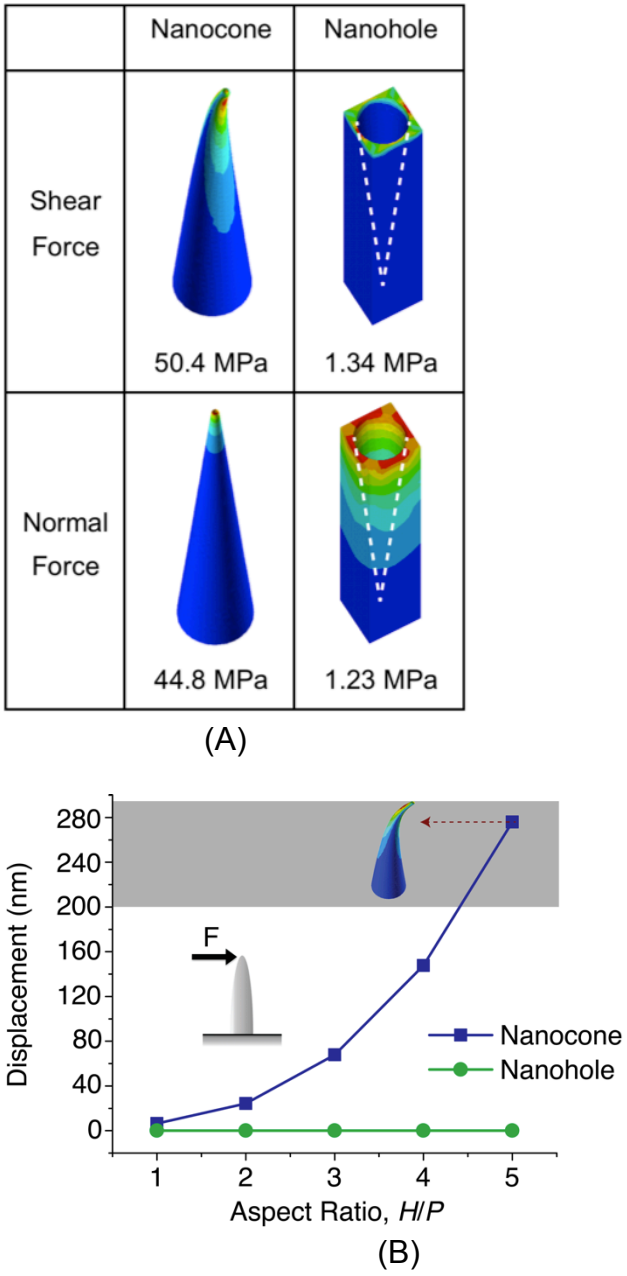

Figure 3. Mechanical robustness calculated by finite element method (FEM): (A) Stress distribution in a nanocone and a nanohole structure (fabricated from PUA, Young's modulus $E \approx$ 400 MPa) resulting from a typical shearing or normal finger force (4 N) applied at the top over a circular area with a radius of 5mm. The numerical values represent the maximum Von Mises stresses for each case; (B) Maximum tip deflections of a nanocone and a nanohole structure (P = 200 nm) under a lateral shearing force for different aspect ratio of nanocones and nanoholes. The gray shaded region indicates a tip displacement that is greater than the pitch of the nanocones.

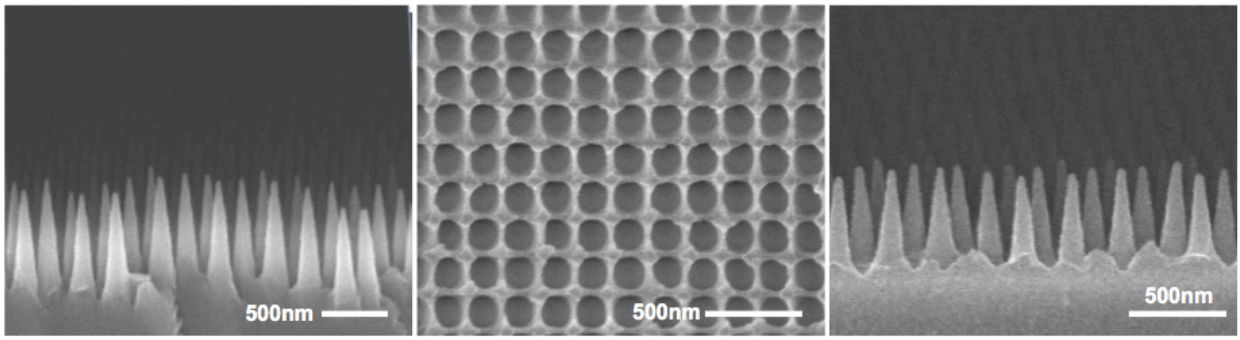

Figure 4. SEM images of (A) side view of a silica mold fabricated using laser interference lithography. (B) Replicated inverted nanocone arrays imprinted in PUA and (C) second generation replicated PUA nanocone arrays. The aspect ratio of the replicated nanostructure is $H/P \cong 4$ with tip radius $r_{tip} \cong 20$ nm.

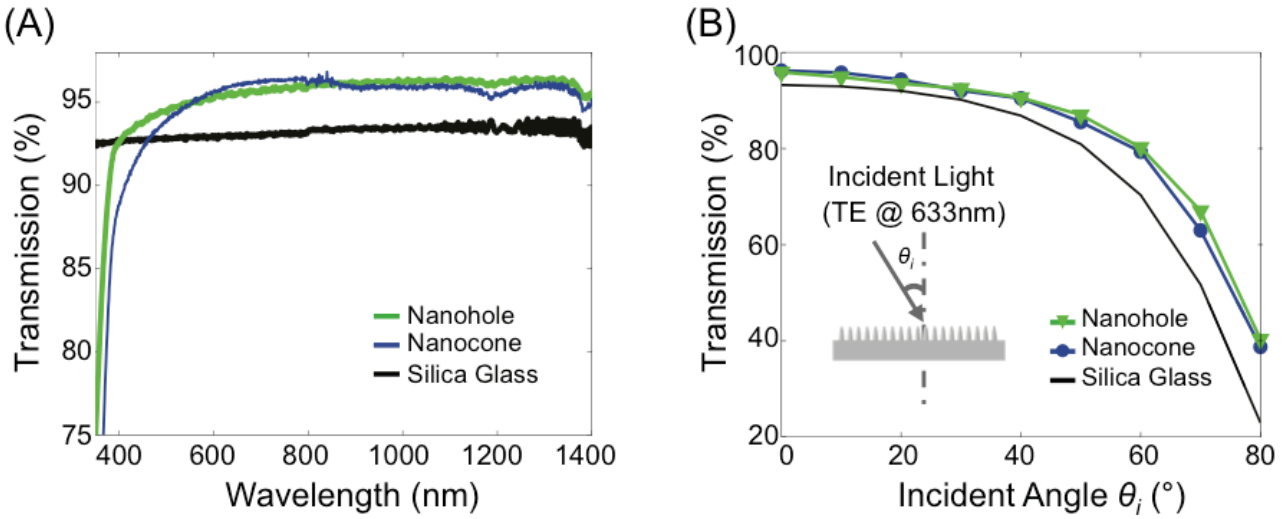

Figure 5. Enhanced optical transmission of the nanotextured surfaces. (A) Measured broadband transmission over a wide range of wavelength (350 nm < λ < 1400 nm) and (B) optical transmission for transverse electric (TE) polarized light through the nanotextured and flat fused silica surfaces is measured by changing the incident angle of a laser source whose wavelength is 633 nm. At an angle of $\theta_i = 80°$, the transmission of the nanohole array is $T = 40.3\%$, but has dropped to $T = 23.0\%$ for the flat silica glass. Each angular point was averaged automatically by the power meter (Newport, 2832-C) over 100 repeated measurements with standard deviation of less than 0.01%.

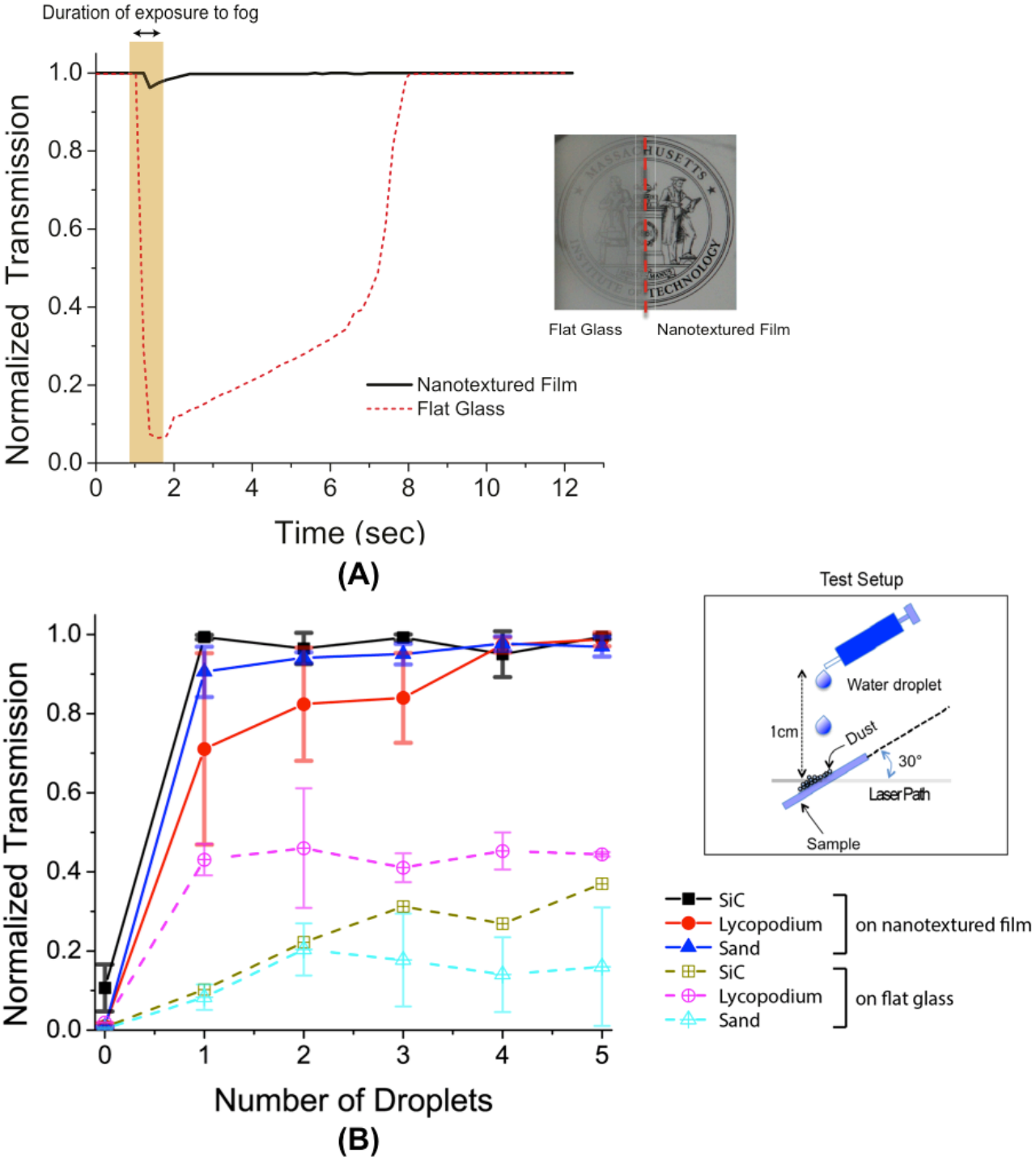

Figure 6. Optical transmission measurements showing (A) anti-fogging behavior of superhydrophilic inverted nanocone surfaces and (B) self-cleaning behavior of water-repelling inverted nanocone surfaces with three different types of powders coated with thickness of more than 0.5 mm (SiC particles, Lycopodium spores and white sand grains with average diameters of 10 µm, 30 µm and 100 µm, respectively). The error bars were determined by repeating the measurements three times each; the large deviations are because of the dynamic nature of the measurement; the precise location of the droplet impacts, the initial uniformity of the powder on the

surface, and the evolution of the droplets and contaminants after droplet deposition could only be controlled with limited precision.

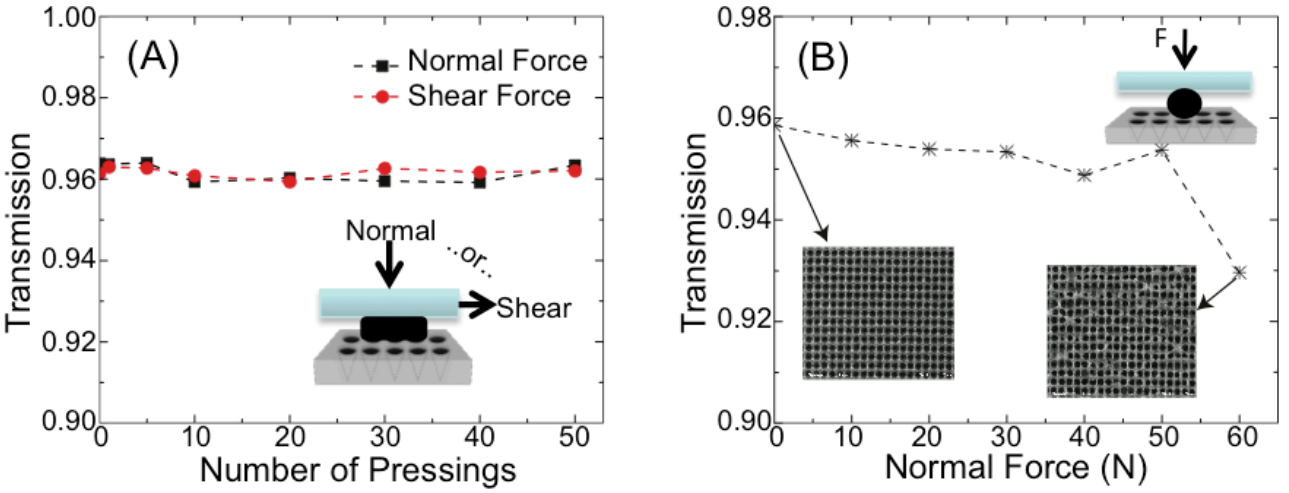

Figure 7. Mechanical robustness test of PUA surfaces textured with inverted nanocone arrays. (A) Optical transmissivity of the nanotextured surface after applying a contact force of 4 N in the normal and shearing directions of the nanotextured surface through a latex rubber pad (dimension 8.9 mm × 8.9 mm) repeatedly; (B) after applying normal force through a Neoprene rubber ball (Young's modulus $E_{np} \cong 5.5$ MPa and radius $R_{np} = 4.8$ mm) up to 60 N (Corresponding contact pressure ≅ 3 MPa, calculated using Hertz contact pressure).[20] The insets show the SEM images of the egg-crate nanotexture before and after applying the force.

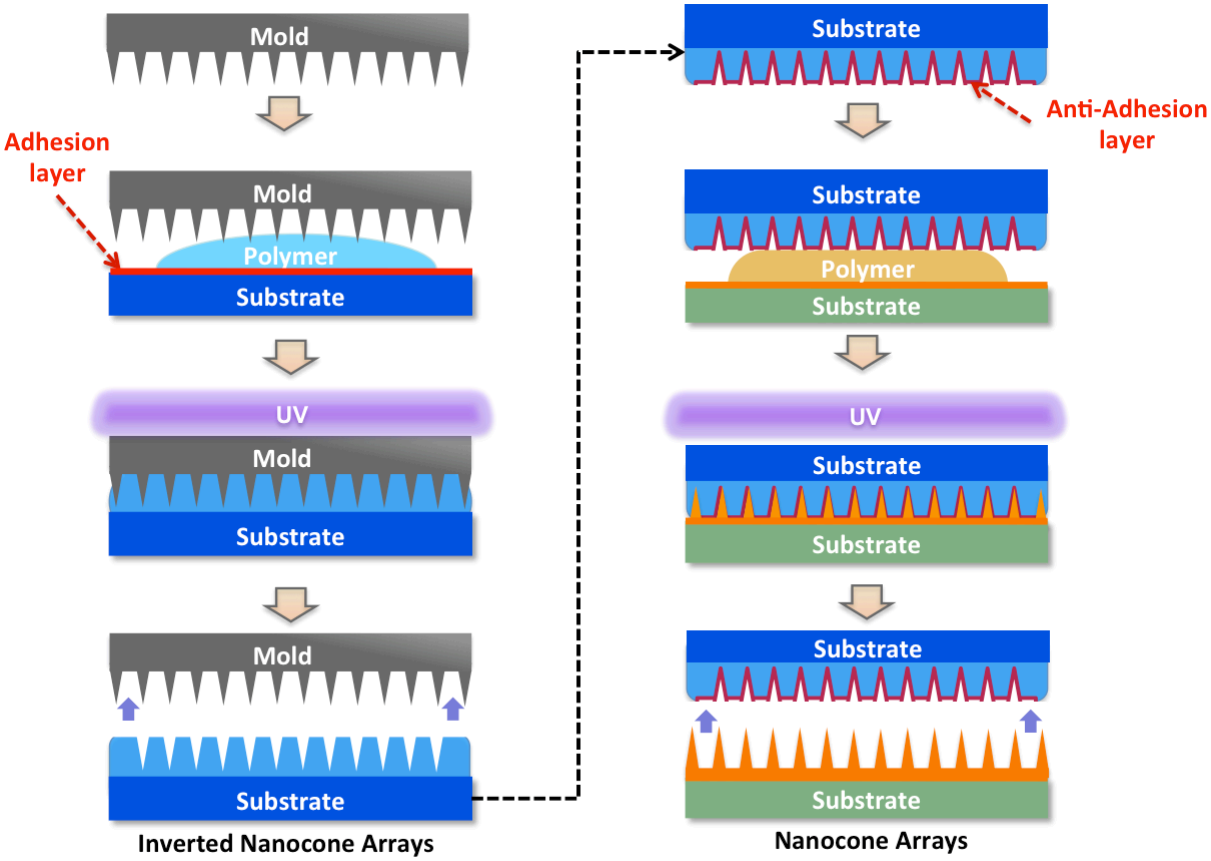

Figure 8. Schematic representation of the fabrication process showing (A) the inverted nanocone arrays replicated from the original nanocone master, and (B) second generation of replicated nanocone arrays formed and released using an anti-adhesion layer in UV-curable poly urethane acrylate (PUA).[25]

Submitted to small

Supporting Information

for *Small*, DOI: 10.1002/ smll.201303051R1

Multifunctional Inverted Nanocone Arrays for Non-wetting, Self-cleaning Transparent Surface with High Mechanical Robustness

*Jeong-Gil Kim, Hyungryul J. Choi, Kyoo-Chul Park, Robert E. Cohen, Gareth H. McKinley, and George Barbastathis**

Section 1. Computation of the change in the Gibbs free energy density for prediction of thermodynamic stability of wetting states and apparent contact angle on an inverted nanocone surface structure.

The imbibition of liquid (water) into the inverted nanocone geometry used in this work leads to a change in the thermodynamic free energy of the liquid droplet-air-textured solid surface system. The gain (or loss) in the overall free energy associated with the liquid penetration[1, 2] can be represented in terms of a contour map (Figure 2) showing the relative value of the Gibbs free energy density (G^*) with respect to the normalized penetration depth (z/H) and putative apparent contact angle (θ_p^*).[2] It should be noted that the location (in z/H) of the lowest Gibbs free energy density point represents the globally stable wetting state and the corresponding value of θ_p^* predicts the apparent contact angle (θ^*) of a liquid droplet in the system. We employ the formulation used in previous studies[1, 2] and numerically compute the change in the Gibbs free energy density G^* with respect to a reference state of G_0^* at $z/H = 0$ in consideration of an inverted nanocone geometry shown in Figure 1B and S1. (see the Supporting Information in the work of Tuteja *et al*.[2] for computation steps in a *MATLAB*® (The Mathworks Inc.) code)

$$G^* = \gamma_{lv}\pi R^2(-2-2\cos\theta_p^* - \sin^2\theta_p^*(r_\phi\phi_s\cos\theta_p^* + \phi_s - 1))/4\pi R_0^2 \quad \text{(S1)}$$

$$R = R_0(4/(2-3\cos\theta_p^* + \cos^3\theta_p^*))^{1/3} \quad \text{(S2)}$$

where γ_{lv} = liquid-vapor interfacial tension, R = radius of the drop in contact with the surface at an angle θ_p^*, R_0 = original radius of drop (at $z/H = 0$), r_ϕ is the roughness of the wetted area and ϕ_s is the area fraction of the liquid-air interface occluded by the solid texture.

To numerically calculate ϕ_s and r_ϕ as a function of z/H, each actual slender nanohole is approximated as an inverted nanocone geometry. It should be noted that $r_\phi\phi_s$ value becomes Wenzel roughness (r_w) when $z/H = 1$.

$$\phi_s = 1-(\pi/4)\left(1-z/H\right)^2 \quad \text{(S3)}$$

$$r_\phi = \left(1-\pi/4\right)+\pi/2\times\left[1-\left(1-z/H\right)^2\right]\sqrt{\left(H/P\right)^2+1/4} \quad \text{(S4)}$$

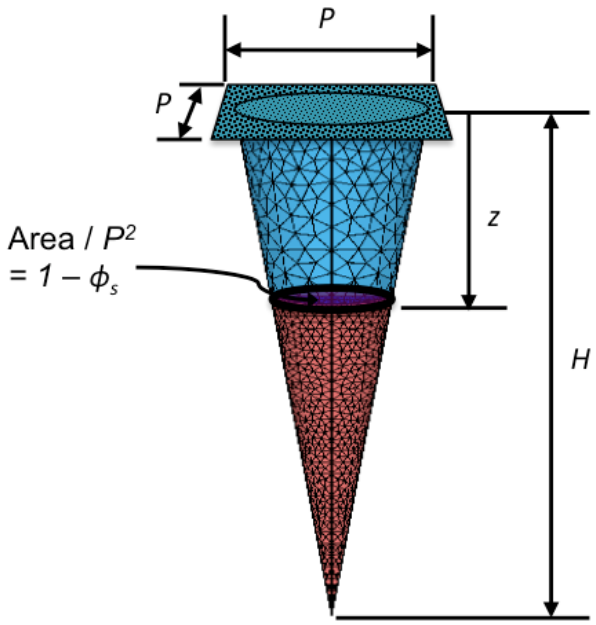

Figure S1. A schematic diagram of an inverted nanocone structure. Solid-liquid and solid-air interfaces are represented by cyan and red colors, respectively.